

Cite this: DOI: 00.0000/xxxxxxxxxx

Universal electronic manifolds for extrapolative alloy discovery

Pranoy Ray^{a,b}, Sayan Bhowmik^c, Phanish Suryanarayana^{b,d}, Surya R. Kalidindi^{a,b} and Andrew J. Medford^{c†}Received Date
Accepted Date

DOI: 00.0000/xxxxxxxxxx

This study presents a computationally efficient framework for accelerated alloy discovery that uses the non-interacting electron density to capture intrinsic structure-property relationships in refractory high-entropy alloys (HEAs). Unlike state-of-the-art approaches relying on expensive, self-consistent density functional theory calculations, our method employs the non-interacting electron density as the primary structural descriptor. By extracting physical features through directionally resolved two-point spatial correlations and compressing them via Principal Component Analysis, we efficiently map the design space. Coupling these descriptors with Bayesian active learning, we achieve a normalized mean absolute error (NMAE) of <2% for the bulk modulus of Al-Nb-Ti-Zr alloys using only 10 training samples. Furthermore, we demonstrate that the model learns an electronic packing manifold that is transferable across distinct chemical species within refractory HEAs. Validated on a distinct 7-component refractory system (Mo-Nb-Ta-Ti-V-W-Zr) containing four elements entirely absent from the training data, the framework enables rigorous zero-shot extrapolation. Moreover, by augmenting the base model with just 20 samples from the target domain, we achieve high-fidelity predictions (NMAE < 3%) for 7-component alloys, reducing data acquisition costs by orders of magnitude compared to standard workflows. These results establish the non-interacting electron density as a rigorous, extrapolative descriptor for vast compositional landscapes.

Introduction

High-entropy alloys (HEAs)^{1–3} encompass a vast compositional design space that offers exceptional tunability for mechanical and thermal properties, yet this combinatorial magnitude renders exhaustive experimental exploration intractable. While Kohn-Sham density functional theory (DFT)^{4,5} offers first-principles accuracy^{6–8}, its large computational cost and $\mathcal{O}(N^3)$ scaling with system size render exhaustive high-throughput screening^{9,10} of HEA compositional spaces computationally prohibitive. Machine learning (ML) surrogates^{11–21} address this by approximating property predictions at reduced cost. Recent efforts have further enhanced sample efficiency through Bayesian active learning^{22–34} and Gaussian Process Regression (GPR)^{35–39}, though their efficacy depends critically on the choice of structural de-

scriptors.

Recent advances^{10,40–42} in physics-based feature engineering have established the electron density field as a robust, chemically agnostic descriptor for atomic structures. These methods are powerful because the converged charge density encodes the quantum mechanical ground state, but this fidelity comes at substantial computational cost. State-of-the-art frameworks, such as the Voxelized Atomic Structure (VAST) method^{43–45}, utilize the fully converged electron density field to quantify structural features via two-point spatial correlations^{10,13,46–49}. While these descriptors achieve high fidelity, they create a fundamental inefficiency: the calculation of the electronic ground state via self-consistent field (SCF) iteration, the dominant computational cost in static DFT, must be completed for every candidate structure merely to generate input features for the surrogate model. This limits the primary value proposition of machine learning surrogates, as the computational budget required for feature generation becomes comparable to that of directly computing the target property.

To address this bottleneck, we investigate the efficacy of the non-interacting valence electron density, hereafter referred to as pseudo-density. In practice, the pseudo-density represents the superposition of isolated valence electron densities corresponding to atoms placed at the Special Quasirandom⁵⁰ (SQS) lattice

^a George W. Woodruff School of Mechanical Engineering, Georgia Institute of Technology, Atlanta, GA, USA

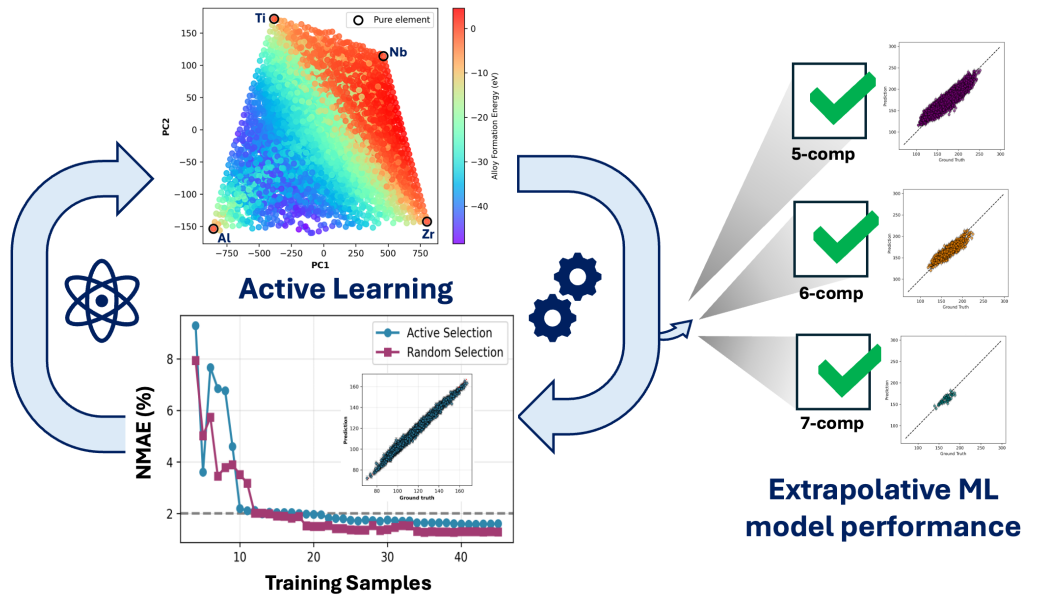
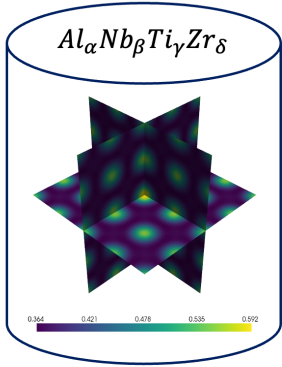
^b School of Computational Science and Engineering, Georgia Institute of Technology, Atlanta, GA, USA

^c School of Chemical and Biomolecular Engineering, Georgia Institute of Technology, Atlanta, GA, USA

^d School of Civil and Environmental Engineering, Georgia Institute of Technology, Atlanta, GA, USA

† Corresponding Author: ajm@gatech.edu

Universal Electronic Manifold



Graphical Abstract

sites, determined via Vegard's Law to bypass equilibrium geometry optimization, with no subsequent electronic relaxation. By eliminating the iterative SCF cycle, the presented approach reduces the computational cost of feature generation by orders of magnitude compared to fully converged DFT⁴⁴, while preserving essential chemical and valence electron information. Our approach rests on the premise that in HEAs, property variance is driven by chemical composition wherein superimposed valence densities could act as an effective descriptor. Consequently, the pseudo-density should retain sufficient physical fidelity for predictive modeling; a hypothesis supported by recent work¹⁴. Furthermore, because these descriptors are derived via unsupervised learning, solely from atomic configuration and elemental identity independent of any target property, we hypothesize they form a 'universal' representation capable of predicting disparate physical quantities, e.g., mechanical and electronic properties, without feature re-engineering. Crucially, we further posit that this physics-based fidelity offers a solution to the challenge of transferability. We hypothesize that because pseudo-electron densities capture the fundamental spatial packing and overlap of valence electrons, they effectively form a 'universal manifold' for refractory alloys. This would allow a model trained on a lower-order system, e.g., 4-component, to predict properties of higher-order systems, e.g., 7-component, without additional training.

In this work, we present a framework integrating pseudo-density descriptors: quantified via two-point spatial correlations and PCA, with Gaussian Process Regression (GPR) driven Bayesian active learning. We validate the approach on the Al-Nb-Ti-Zr system (\mathcal{D}_4), achieving $R^2 > 0.97$ for both bulk modulus and alloy formation energy. Notably, the bulk modulus model attains a normalized mean absolute percentage error (NMAE) of $< 2\%$ using only 10 training samples, surpassing benchmarks utilizing converged densities. We further demonstrate extrapolative power by applying the \mathcal{D}_4 -trained model to a distinct 7-

component system (\mathcal{D}_7 : Mo-Nb-Ta-Ti-V-W-Zr). The framework enables robust zero-shot prediction, and with the augmentation of just 20 actively selected \mathcal{D}_7 samples, recovers high-fidelity predictions (MAPE $< 3\%$), establishing pseudo-density as a rigorous descriptor for accelerated HEA discovery.

Data Curation and Design Space

This study investigates the quaternary Al-Nb-Ti-Zr refractory HEA system, spanning a large compositional space defined by:

$$\mathcal{D}_4 = \{Al_\alpha Nb_\beta Ti_\gamma Zr_\delta \mid \alpha, \beta, \gamma, \delta \in \{0, 4, \dots, 128\}, \alpha + \beta + \gamma + \delta = 128\}. \quad (1)$$

This discrete set yields a total of 6,545 unique structures when including elemental, binary, ternary, and quaternary compositions, and 4,495 alloys when restricted to the quaternary space. To validate the extrapolative transferability of the model, we leverage the distinct 7-component domain (\mathcal{D}_7), defined by the set:

$$\mathcal{D}_7 = \{Mo_\alpha Nb_\beta Ta_\gamma Ti_\delta V_\epsilon W_\zeta Zr_\eta \mid \alpha, \dots, \eta \in \{0, 15, 23, 30, 38, \dots, 105, 128\}, \alpha + \beta + \gamma + \delta + \epsilon + \zeta + \eta = 128\}. \quad (2)$$

The ground truth values for bulk modulus and alloy formation energy were obtained from the converged DFT dataset established by Barry et al.^{43,44}. Note that the alloy formation energies were available only for \mathcal{D}_4 .

Background

Pseudo-Density

In this framework, the material structure is defined by the pseudo-density field, $\rho_{\text{pseudo}} : \Omega \rightarrow \mathbb{R}_{\geq 0}$, where $\Omega \subset \mathbb{R}^3$ represents the

spatial domain of the atomic system. This framework’s key innovation is bypassing the computationally expensive SCF cycle. While converged densities require iterative Hamiltonian diagonalization, pseudo-densities are constructed via a single-shot superposition of isolated atom electron densities^{51,52}, where each element contributes its valence electron density according to its specific spatial distribution. This effectively decouples feature generation from the computationally expensive electronic relaxation process.

We modeled the random solid solution behavior of refractory HEAs through Special Quasirandom Structures (SQS)⁵⁰ generated via the Alloy Theoretic Automated Toolkit (ATAT)⁵³ using *sqsgenerator*⁵⁴. All SQS structures were generated with the same set of lattice parameters. For each structure, the pseudo-density was computed using valence electron densities in the Optimized Norm-Conserving Vanderbilt (ONCV)⁵⁵ pseudopotential files from the SPMS set⁵⁶. We employed the PBE exchange-correlation functional inherent to these pseudopotentials. While higher-level functionals (e.g., SCAN or Hybrids) offer improved energetic accuracy for ground-state calculations, the non-interacting pseudo-density relies primarily on the spatial topology of valence orbitals rather than absolute energy minimization. The Generalized Gradient Approximation (GGA)⁵⁷ sufficiently captures the characteristic atomic radii and overlap features required for this topological mapping, while maintaining consistency with standard high-throughput screening libraries. The pseudo-density was mapped onto a 3D real-space grid closely mimicking the implementation in the M-SPARC^{58,59} and SPARC^{60,61} electronic structure codes. Critically, the generation of ρ_{pseudo} bypasses the iterative SCF procedure⁶², hence the computational cost is significantly reduced compared to fully converged DFT calculations, thereby facilitating high-throughput screening of complex composition spaces.

Feature Engineering using Spatial Correlations

To quantify the salient structural features governing the material response, we employ directionally resolved two-point spatial correlations^{46,63}. This measure captures spatial positioning of charge density features, creating a translationally invariant descriptor. For computational efficiency, the discrete two-point autocorrelations, f_r , are calculated using Fast Fourier Transforms (FFT)^{64–66} on a discretized grid:

$$f_r = \frac{1}{|S|} \mathcal{F}^{-1} \left[\mathcal{F} \left(\sqrt{\rho_{\text{pseudo}}} \right) * \mathcal{F} \left(\sqrt{\rho_{\text{pseudo}}} \right) \right], \quad (3)$$

where \mathcal{F} denotes the discrete Fourier transform operation, the asterisk (*) indicates the autocorrelation operation, and S represents the set of voxel indices. The spatial domain for ρ_{pseudo} was discretized with a fixed voxel size of $\lambda = 0.2 \text{ \AA}$, as done in previous work⁴⁴ utilizing converged electron charge densities. This approach enables efficient computation of spatial correlations for high-throughput screening.

The resulting high-dimensional autocorrelation vectors are projected onto a low-dimensional feature space using Principal Component Analysis (PCA). This projection compresses the feature

space while preserving the variance that distinguishes different atomic configurations.

Dimensionality Reduction using PCA

We apply PCA to the autocorrelation feature vectors to obtain a compact, low-dimensional representation. In the combined feature space of both datasets, the first three principal components capture approximately 50% of the total variance, with the first component accounting for 40%. The PCA basis vectors systematically decompose the structural hierarchy: the first principal component captures the mean charge density, while subsequent components resolve the complex spatial patterns associated with local atomic disorder.

The low-dimensional representation maintains the physical hierarchy of the alloy system. As illustrated in Figure 1 for \mathcal{D}_4 , the data points naturally arrange into a trapezoidal geometry where pure elements occupy the vertices and all alloy compositions fill the interior volume. This smooth variation of principal component scores across the composition space facilitates robust interpolation and accurate property prediction for unexplored alloy stoichiometries. Because this dimensionality reduction is unsupervised, the resulting descriptors are property-agnostic and can be reused to train independent models for different target properties, e.g., mechanical or thermodynamic, without re-computation. Notably, this unsupervised PC projection remains fixed regardless of the target property, allowing the same structural map to be colored by distinct physical responses, e.g., bulk modulus or alloy formation energy: see Figure 1 to reveal property-specific manifolds. Based on the variance analysis, we truncate the descriptor space to the first three principal components* for all subsequent regression modeling. These three components sufficiently capture the structural hierarchy required for property prediction, as evidenced by the model performance.

Impact of Structural Relaxation on Manifold Topology

A critical and counter-intuitive finding of this work is that structural descriptors derived from initial SQS configurations with a uniform, common lattice constant yield a more cohesive feature space than those derived from fully relaxed geometries. Figure 1 visualizes the Principal Component space for the initial uniform SQS structures compared to those relaxed via VASP^{67–70} and MACE⁷¹ (see plots c, d, e and f in Supplementary Figure S1). Here, relaxation refers to the full optimization of both internal ionic coordinates and cell volume. The uniform SQS data forms a continuous, cohesive simplex, where the variance is driven purely by the combinatorial arrangement of chemical species. In contrast, the relaxed structures fracture into a distinct, disjoint, hyper-branched topology.

This fracturing is fundamentally driven by the loss of volumetric uniformity during relaxation. In the uniform initial state, a globally constant spatial metric is enforced for the two-point spatial statistics across all samples. During relaxation, individual lat-

* see Supplementary Figure S1 (a) and (b)

tice parameters deviate significantly from this uniform baseline, rendering the spatial metric sample-dependent. As the concentration of larger atoms like Zr increases (Zr’s ionic radius is approximately 10% larger than that of Al, Nb, and Ti), the lattice undergoes significant global cell expansion to minimize steric hindrance.

This phenomenon can be rigorously understood by considering the variance maximization objective of PCA acting on absolute spatial coordinates. Because the f_r are computed on an absolute real-space grid, global cell expansion physically dilates the interatomic distances between charge density peaks. Consequently, the variance is dominated by different lattice constants scaling the spatial metric, rather than strictly chemical variations. PCA aggressively captures this spatial dilation, fracturing the manifold into discrete arms. When the relaxed PC space is colored by the final relaxed lattice parameter, the distinct branches stratify perfectly by cell volume, with the arms corresponding to discrete lattice parameter bands (see Figure S3) scaling from approximately 12.8 Å to 14.2 Å. The terminal tips of these disjoint manifolds correspond exactly to the absolute structural limits of the dataset, specifically the highly expanded Zr-rich compositions.

To rigorously validate that this non-uniform volumetric scaling is the primary driver of the fracturing, we performed an ablation test where the absolute-grid f_r were divided by the cell volume (a^3) before performing PCA (see Figure S4). This operation effectively normalizes the magnitude-dependent variance driven by the cell expansion. Suppressing this volume-dependent information caused the previously disjoint branches to coalesce back into a single, continuous cluster. This mathematically confirms that the geometric relaxation, specifically the variance in the final relaxed lattice constants, is responsible for the manifold fracturing.

It is worth noting that if the f_r were computed on a normalized grid using relative fractional coordinates (x/a), the affine volume expansion would be factored out, isolating the variance purely to local ionic displacements. However, by using the initial system’s pseudo-density with a uniform lattice constant on an absolute grid, we inherently bypass both the volumetric and ionic strain artifacts. By enforcing this globally constant spatial metric, we effectively treat the ideal lattice as a canonical reference state. This enables the Gaussian Process³⁶ to interpolate across a smooth manifold ($f(\text{chemistry}) \rightarrow P_{\text{property}}$) without the interference of high-variance geometric noise introduced by relaxation.

Model Building

Gaussian Process Regression

We employ Gaussian Process Regression (GPR)⁷² to model the mapping between the low-dimensional structural features (PC scores) and the material properties. GPR provides a non-parametric, probabilistic framework that yields both a predictive mean and a variance, which is essential for uncertainty quantification. The covariance between inputs is computed using the Automatic Relevance Determination Squared Exponential (ARDSE)⁷³ kernel:

$$k(\mathbf{x}, \mathbf{x}') = \sigma_s^2 \exp \left[-\frac{1}{2} \sum_{d=1}^D \frac{(x_d - x'_d)^2}{l_d^2} \right] + \sigma_n^2 \delta_{\mathbf{x}\mathbf{x}'} \quad (4)$$

where σ_s^2 scales the output variance, l_d represents the characteristic length-scale for feature dimension d , and σ_n^2 accounts for observation noise. The ARDSE kernel allows the model to inherently determine the relevance of each principal component, weighting them according to their influence on the target property. This choice reflects the expectation that different principal components encode distinct physical scales, e.g., mean density versus local disorder, and allows the GP to adapt its sensitivity accordingly.

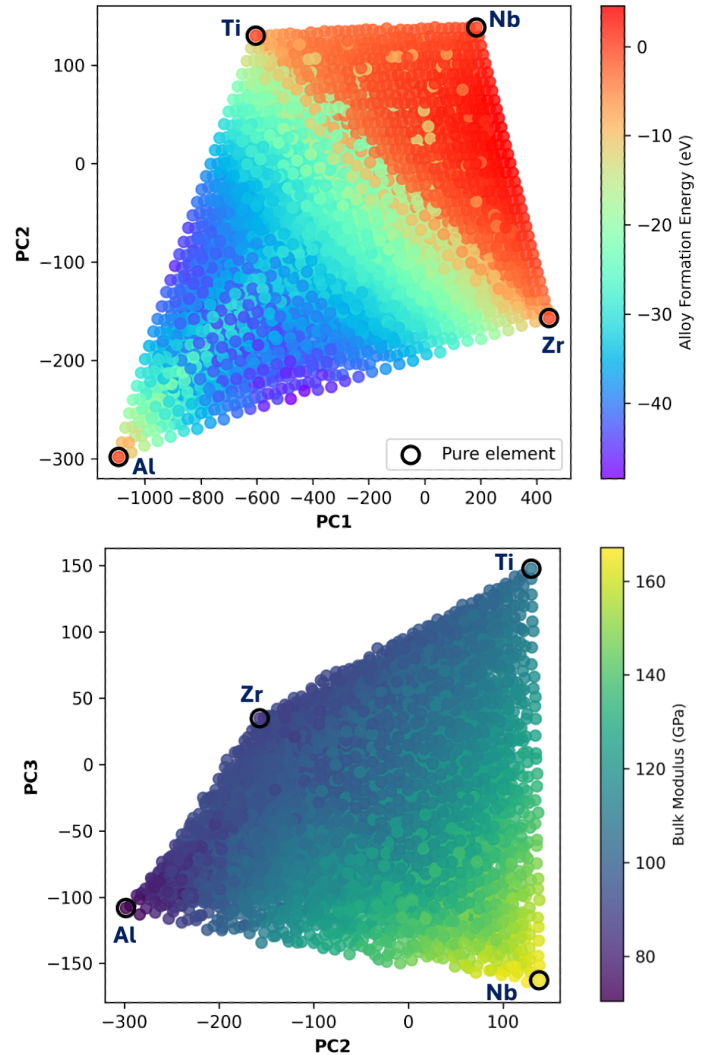


Fig. 1 Principal component visualization of the AlNbTiZr composition space (\mathcal{S}_4). The 2D projections of the first three PC scores reveal a trapezoidal arrangement where elemental compositions reside at the vertices and the alloys populate the interior, indicating that the pseudo electron density descriptors preserve the chemical and structural hierarchy of the composition space. The 3D projections are located in Supp. Figure S1

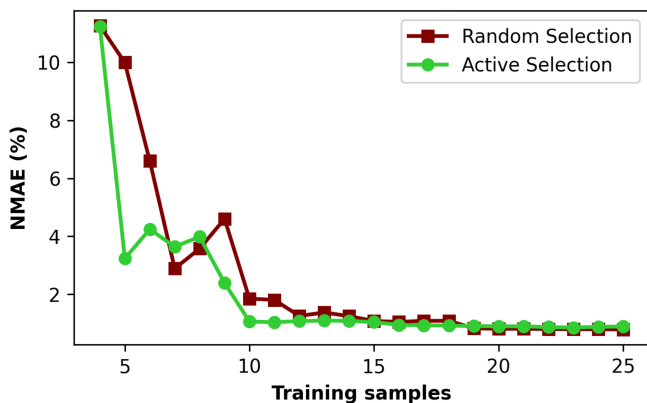


Fig. 2 Convergence of bulk modulus prediction error (for \mathcal{D}_4) with training set size: NMAE versus number of training samples for active and random selection strategies. The active learning strategy using pseudo-density features converges to $<2\%$ error within 10 samples, demonstrating that the non-relaxed field contains sufficient information to guide the acquisition function effectively.

Bayesian Experiment Design

To minimize the computational expense of data generation, we utilize a Bayesian active learning strategy driven by a relative-uncertainty acquisition function inspired by information-based design^{74,75}. Specifically, the acquisition selects candidate structures that maximize the ratio of predictive uncertainty to the predicted magnitude:

$$I(\mathbf{x}) = \frac{\sigma(\mathbf{x})}{\mu(\mathbf{x})} \quad (5)$$

where $\mu(\mathbf{x})$ and $\sigma(\mathbf{x})$ are the predictive mean and standard deviation provided by the GPR model, respectively. In each iteration, the algorithm identifies the k structure with the highest $I(\mathbf{x})$ for ground-truth evaluation. In a prospective discovery campaign, this step would selectively trigger DFT calculations for these specific unlabelled candidates, thereby augmenting the training set with high-fidelity data only where strictly necessary. While active learning strategies have been successfully applied to descriptors derived from converged densities⁴⁴, such workflows inherently face a "pre-computation" bottleneck: the computationally expensive SCF cycle must be completed for every candidate structure merely to generate the input features for the surrogate model. In contrast, our pseudo-density framework eliminates this redundancy, enabling the rapid, low-cost scanning of the entire candidate pool prior to triggering any expensive DFT calculations. This iterative process (see Figure 3) empirically leads to rapid convergence by prioritizing sampling in regions in the design space where the predictive confidence is lowest.

Extrapolative Validation Protocol

To rigorously assess the transferability of the pseudo-density descriptors, we designed a disjoint training-testing protocol. The GPR model was actively trained exclusively on samples from the lower-order domain \mathcal{D}_4 (Al-Nb-Ti-Zr). This model was then frozen and tasked with predicting the properties of the full extrapolation domain \mathcal{D}_7 (Mo-Nb-Ta-Ti-V-W-Zr) without any re-training or exposure to the new chemical elements. This zero-shot trans-

fer protocol evaluates whether the learned regression mapping $f: \mathbf{PC} \rightarrow K$ generalizes across chemically distinct refractory systems without re-training, fine-tuning, or element-specific feature engineering. Successful extrapolation would imply that the pseudo-density descriptor encodes a universal electronic overlap manifold transcending atomic labels.

Error metrics

Across all experiments, model performance is quantified using the mean absolute error (MAE), normalized MAE (NMAE), mean absolute percentage error (MAPE), and coefficient of determination (R^2). For a set of N predictions $\{\hat{y}_i\}$ and corresponding ground-truth values $\{y_i\}$, these are defined as

$$\text{MAE} = \frac{1}{N} \sum_{i=1}^N |\hat{y}_i - y_i|, \quad (6)$$

$$\text{NMAE} = \frac{\text{MAE}}{\bar{y}} \times 100\%, \quad (7)$$

where \bar{y} is the mean of the ground-truth values $\{y_i\}$.

Results and Discussion

Performance on Bulk Modulus predictions

The GPR model demonstrates high predictive accuracy for the bulk modulus across the complete compositional dataset (\mathcal{D}_4). The active learning campaign is initialized with a minimal seed of 4 randomly selected samples, followed by iterative acquisition. As shown in Figure 2, the model stabilizes rapidly, achieving an NMAE of $<2\%$ with only 10 total training samples (4 seed + 6 active). This efficiency highlights a significant advantage over competing descriptor frameworks. While state-of-the-art methods typically require significantly larger datasets (10^2 – 10^3 samples) or approximately 26 samples for converged charge density descriptors⁴⁴ to reach convergence, our approach achieves this fidelity with fewer samples and orders of magnitude lower computational cost for feature generation.

The robustness of the pseudo-density descriptor is further evidenced by the performance of random sampling. As summarized in Table 1, even the random selection strategy yields high accuracy ($R^2 = 0.98$, MAE = 1.41 GPa) on the full dataset (\mathcal{D}_4). This indicates that the unrelaxed pseudo-density manifold is naturally well-correlated with the mechanical response, such that complex active learning acquisition functions are not strictly required to achieve good global accuracy; though they still offer superior efficiency in the low-data limit (Figure 2). The parity plot in Figure 4(a) confirms this strong linear correlation ($R^2 = 0.98$) across the full range of 80 GPa to 160 GPa, confirming that the superposition of non-interacting electron densities contains sufficient physical information to resolve variations in mechanical stiffness without systematic bias.

Performance on Alloy Formation Energy predictions

Crucially, this physics-based feature set exhibits high transferability across properties. The same 3-PC pseudo-density features accurately predict both mechanical stiffness (bulk modulus) and

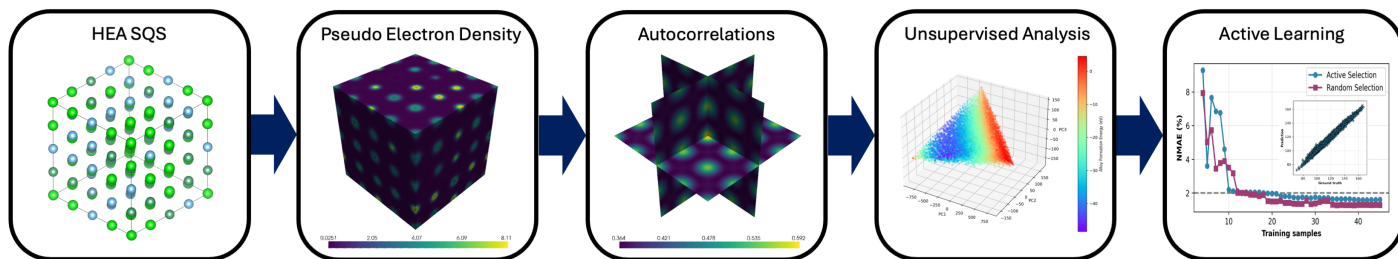


Fig. 3 The end to end Bayesian Experiment Design workflow used to train \mathcal{D}_4

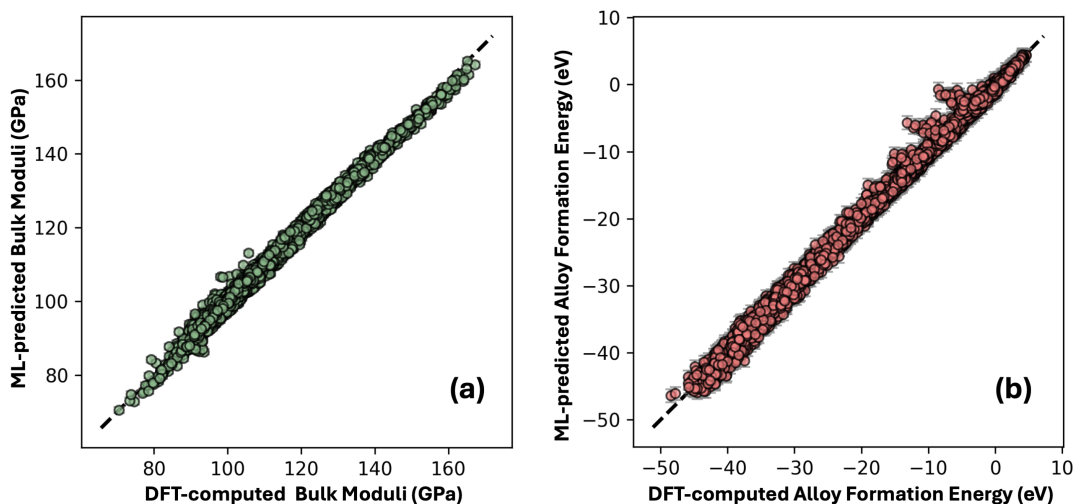


Fig. 4 Parity plots of predicted versus DFT-computed properties for the remaining samples in \mathcal{D}_4 . (a) Bulk modulus predictions using a model trained on actively selected samples. (b) Alloy formation energy predictions using a distinct GPR model trained on the same 3-PC pseudo-density descriptor inputs.

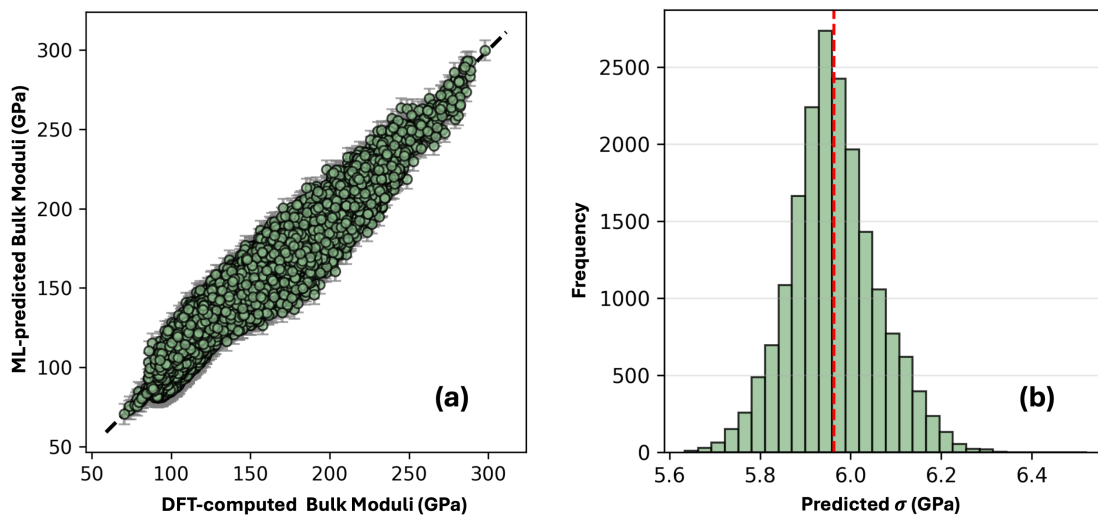


Fig. 5 (a) Extrapolative parity plot assessing the transferability of the pseudo-density descriptor. The model was trained exclusively on the 4-component Al-Nb-Ti-Zr system (\mathcal{D}_4) and tasked with predicting the bulk moduli of the 7-component system (\mathcal{D}_7) containing Mo, Ta, V, and W, (b) The histogram (inset/side) illustrates the uncertainty distribution (predicted standard deviation, σ) for the test set, indicating that the model remains well-calibrated even in the extrapolation regime.

thermodynamic stability (alloy formation energy) without modification. Starting with the same initial seed size of 4 samples, the active selection strategy applied to the full compositional space of

\mathcal{D}_4 (Table 1), achieves an MAE of 1.19 eV (2.20% NMAE) with an R^2 of 0.99.

The parity plot in Figure 4(b) confirms this strong correlation

Table 1 Compiled error metrics for bulk modulus and alloy formation energy predictions for all \mathcal{D}_4 compositions (6,545 structures).

Material Property	Strategy	MAE	NMAE (%)	R^2
Bulk Modulus (GPa)	Active	1.50	1.55	0.98
	Random	1.41	1.46	0.98
Alloy Formation Energy (eV)	Active	1.19	2.20	0.99
	Random	1.23	2.33	0.97

using only 18 actively selected training samples. This result indicates that the pseudo electron density spatial correlations effectively capture the local chemical environment variations that dictate the energetic stability of the solid solution. The uncertainty coverage for ΔE_{form} is similarly robust, achieving 88.8% within $\pm 1\sigma$ and 99.8% within $\pm 2\sigma$.

Comparative Performance and Scientific Implications

Table 1 summarizes the compiled error metrics, confirming that the pseudo-density descriptor yields high fidelity ($R^2 \geq 0.98$) with both active and random sampling. While both strategies converge to similar accuracy in the limit, Figure 2 demonstrates that the active learning strategy provides a superior sample efficiency advantage in the low-data regime. The central finding of this study is the demonstration that pseudo electron densities are a sufficient structural descriptor for high-fidelity property prediction in complex alloy systems. PCA projections of the pseudo electron densities naturally recover the trapezoidal geometry of the 4-element structure space (Figure 1), placing elements at the vertices and alloys in the interior. This confirms that atomic packing and chemical identity; both captured by the pseudo-density, dominate the structural hierarchy of HEAs. Electronic relaxation acts predominantly as a local perturbation relative to these primary chemical variations, though the geometric variance introduced by ionic relaxation is sufficient to fracture the low-dimensional manifold if not accounted for (as confirmed by both PCA and Partial Least Squares analyses). This indicates that for these HEA solid solutions, the electronic environment is dominated by the initial, superposition of atomic charges, and the subsequent self-consistent electronic relaxation introduces differences that are subordinate to the chemical variations across the design space. By replacing the converged density with the pseudo-density, the framework effectively decouples the feature generation step from the most computationally demanding part of the DFT calculation. This combination of eliminating the SCF bottleneck for feature generation and reducing the required number of training samples substantially enhances the feasibility of high-throughput computational materials discovery for HEAs. This efficiency gain does not merely accelerate existing workflows; it unlocks regimes previously inaccessible to DFT-based screening. As demonstrated by the extrapolation results, the pseudo-density descriptor creates a transferable feature space that bridges distinct chemical systems. By projecting the 4-component and 7-component datasets into the same Principal Component space (as discussed in the Methods), we observe that they occupy overlapping manifolds. This indicates that the model predominantly learns electronic packing

rules rather than overfitting to element-specific labels, enabling more rapid exploration of combinatorial spaces (including 5+ component systems) without the need to retrain on every new element. The capability to achieve high accuracy for both bulk modulus and formation energy with minimal training data using a low-cost descriptor represents a critical step towards realizing true high-throughput screening of the vast compositional space.

Generalization to Higher-Order Systems

To rigorously test the physical fidelity of the pseudo-density descriptor, we evaluated the model’s ability to extrapolate to the broader chemical space \mathcal{D}_7 . We first established a robust base model trained on a budget of 200 samples from the 4-component domain \mathcal{D}_4 . While the previous section demonstrated that 10 samples suffice for in-domain screening, this larger training budget was employed here to ensure the model fully captures the electronic manifold’s topology prior to extrapolation. This distinct step allows us to decouple the quality of the descriptor from data scarcity effects during zero-shot testing. As shown in Supplementary Figure S6, this base model exhibits non-trivial zero-shot predictive power on the 5-, 6-, and 7-component alloys of \mathcal{D}_7 (Mo-Nb-Ta-Ti-V-W-Zr), despite the presence of four elements (Mo, Ta, V, W) never encountered during training. This confirms the existence of a transferable electronic manifold.

However, to achieve high-fidelity quantitative predictions suitable for materials screening, we employed a few-shot domain adaptation strategy. The base model was augmented with a minimal batch of 20 actively selected samples from the respective higher-order domains. As summarized in Table 2 and illustrated in Figure 6, this rapid adaptation yields significant predictive accuracy. For the 5-component alloys, the model achieves an R^2 of 0.85 and a NMAE of 5.54%. As the chemical complexity increases to 7 components, the model maintains a strong correlation ($R^2 = 0.68$) and a low NMAE of 2.87%. Visually confirmed in Figure 5, the predictions track the $y = x$ line closely. The accompanying uncertainty distribution (Figure 5, right panel) shows a peaked distribution of predicted standard deviations, suggesting the model remains well-calibrated during this expansion.

This result directly addresses a central limitation of many descriptor-based machine learning approaches in materials science, namely the difficulty of extrapolating beyond the chemical species present in the training set. Unlike composition-based descriptors that require explicit knowledge of all constituent elements, the pseudo-density descriptor operates on a transferable electronic packing manifold. Because the local valence overlap environments in \mathcal{D}_7 structurally resemble those in \mathcal{D}_4 (confirmed by the PC-space overlap in Supp. Fig. S2), the regression mapping adapts rapidly to the new chemical labels with minimal data.

Conclusions

We demonstrated that the non-interacting electron density offers a rigorous and scalable alternative to standard DFT-based descriptors for HEA discovery. By decoupling descriptor generation from the SCF bottleneck, this framework effectively reduces the computational investment of high-throughput screening. The inte-

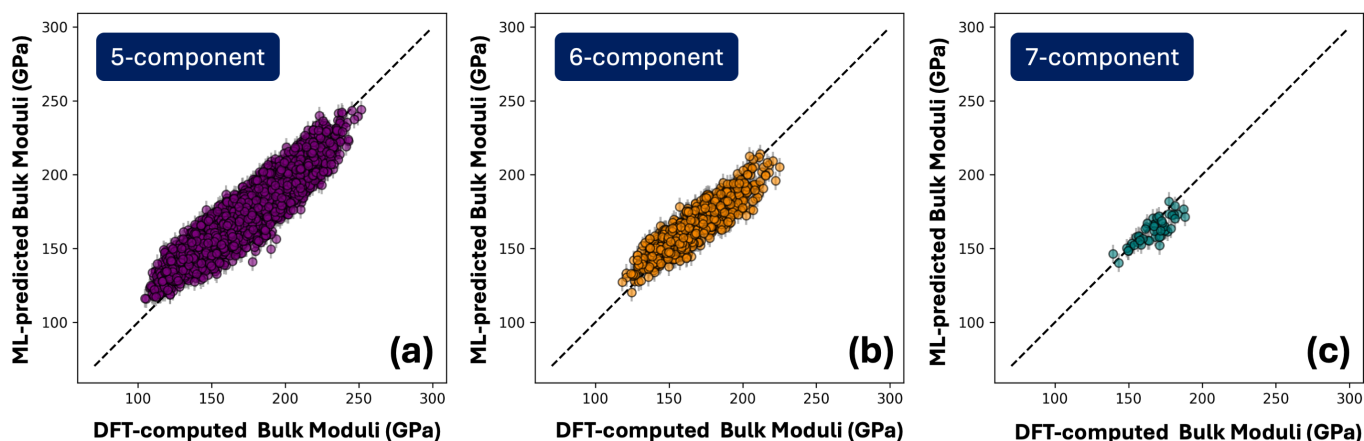


Fig. 6 Breakdown of extrapolative performance by chemical complexity. The parity plots show predictions for (a) 5-component, (b) 6-component, and (c) 7-component alloys within \mathcal{D}_7 . These results were obtained by actively augmenting the base model (trained on \mathcal{D}_4) with just 20 samples from the respective higher-order domains. The high coefficients of determination ($R^2 > 0.82$ for 5- and 6-component systems) demonstrate rapid adaptation to the new chemical space, confirming that the electronic manifold is transferable.

Table 2 Extrapolative performance metrics. The model was trained *only* on 4-component Al-Nb-Ti-Zr and tested on 5, 6, and 7-component alloys containing Mo, Ta, V, and W.

Components	N (Test Samples)	NMAE (%)	MAE (GPa)
5	3675	5.54	9.20
6	882	4.16	7.01
7	49	2.87	4.89

gration of this descriptor with Bayesian active learning demonstrated superior sample efficiency in the Al-Nb-Ti-Zr RHEA system. The framework achieved a NMAE of $<2\%$ for the bulk modulus using only 10 actively selected training samples, surpassing the efficiency of state-of-the-art benchmarks that rely on fully converged densities. Beyond sample efficiency within the training domain, we demonstrated the model’s rigorous capability for chemical extrapolation. A model trained exclusively on the quaternary Al-Nb-Ti-Zr system successfully predicted the bulk moduli of a distinct 7-component system (Mo-Nb-Ta-Ti-V-W-Zr) containing four elements entirely absent from the training set. Furthermore, we demonstrated that augmenting this base model with just 20 samples from the target domain recovers high predictive fidelity (NMAE=2.87% for 7-component alloys). This suggests that the pseudo-density descriptor captures a universal electronic packing manifold that transcends specific element labels, allowing for extremely efficient domain adaptation. Furthermore, we demonstrate the property transferability of this singular feature set; without modification, the descriptors accurately predict alloy formation energies (achieving an R^2 of 0.99 for the full compositional space for \mathcal{D}_4). The robustness of the approach was further validated through uncertainty quantification, which provided reliable confidence bounds for the bulk modulus, achieving robust uncertainty calibration as evidenced by the peaked distribution of predicted standard deviations (Figure 4b and 5b). For the alloy formation energy, the coverage was even closer to nominal, with 88.8% and 99.8% of the data falling within $\pm 1\sigma$ and $\pm 2\sigma$, re-

spectively. Collectively, these results validate the voxelized atomic structure approach using pseudo-densities as a practical route to decoupling descriptor generation from the most computationally demanding stages of DFT.

The overall reduction in computational investment by lowering the requisite DFT calculations via active learning, facilitates the extensive exploration of vast compositional landscapes. Avenues for future research include: (i) validating transferability beyond BCC crystal structures, e.g., FCC, HCP systems, (ii) incorporating temperature-dependent properties via on-the-fly machine-learned molecular dynamics^{76,77}, and (iii) extending the framework to predict functional properties, e.g., thermal conductivity, oxidation resistance, critical for high-temperature applications. Nonetheless, the demonstrated capacity for zero-shot chemical extrapolation marks a significant step toward truly autonomous materials discovery pipelines.

Author contributions

Pranoy Ray: Conceptualization, Methodology, Software, Validation, Formal analysis, Investigation, Data curation, Writing – original draft, Writing – review & editing, Visualization. **Sayan Bhowmik:** Investigation, Software, Validation, Formal analysis, Writing – review & editing. **Phanish Suryanarayana:** Conceptualization, Methodology, Validation, Resources, Writing – review & editing, Supervision, Project administration, Funding acquisition. **Surya R. Kalidindi:** Conceptualization, Methodology, Validation, Resources, Writing – review & editing, Supervision, Project administration, Funding acquisition. **Andrew J. Medford:** Conceptualization, Methodology, Validation, Resources, Writing – review & editing, Supervision, Project administration, Funding acquisition.

Acknowledgements

PR and SK acknowledge support from NSF DMREF Award 2119640. SB, PS, and AJM gratefully acknowledge the support of the U.S. Department of Energy, Office of Science under grant

DE-SC0023445. The authors acknowledge Dr. Matthew C. Barry for providing the dataset for this work through his PhD thesis⁴².

Data availability

All scripts for feature engineering (computing pseudo electron densities & spatial correlations), model training,

and post-processing (uncertainty analysis) are available at <https://github.com/pranoy-ray/AlloyDiscovery>.

Conflicts of interest

There are no conflicts to declare.

Supplementary Information

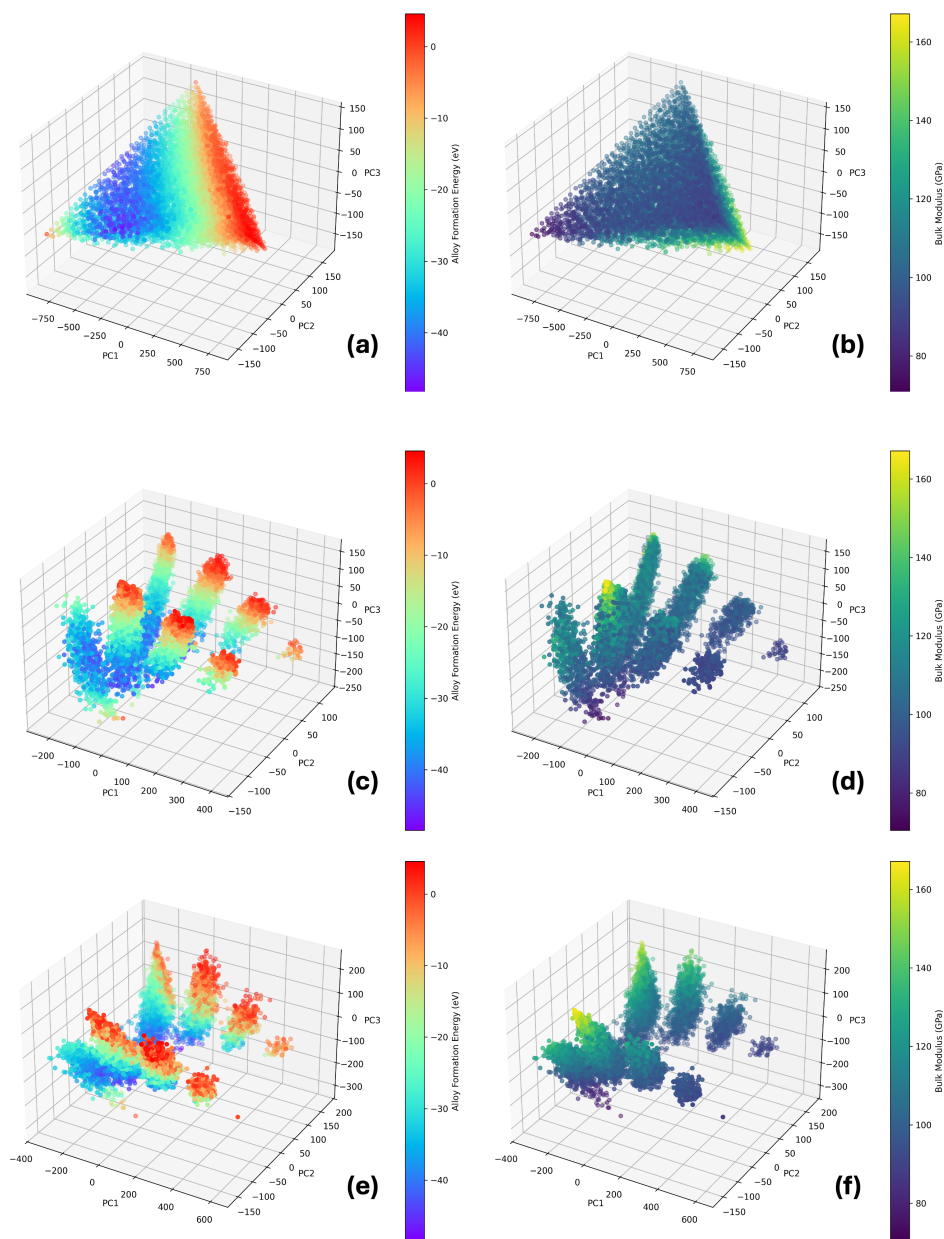


Fig. S1 Principal Component scores (colored by the respective properties) for the relaxed (a, b) SQS (unrelaxed), (c, d) VASP (relaxed), and (e, f) MACE (relaxed) structures of \mathcal{D}_4 . The unrelaxed SQS data forms a continuous, dense simplex, whereas the relaxed structures fracture into disjoint, and distinct element-specific arms due to strain-induced geometric distortions. The smooth topology of the unrelaxed manifold acts as a canonical reference state, facilitating superior GPR performance by minimizing the high-variance geometric noise introduced by relaxation.

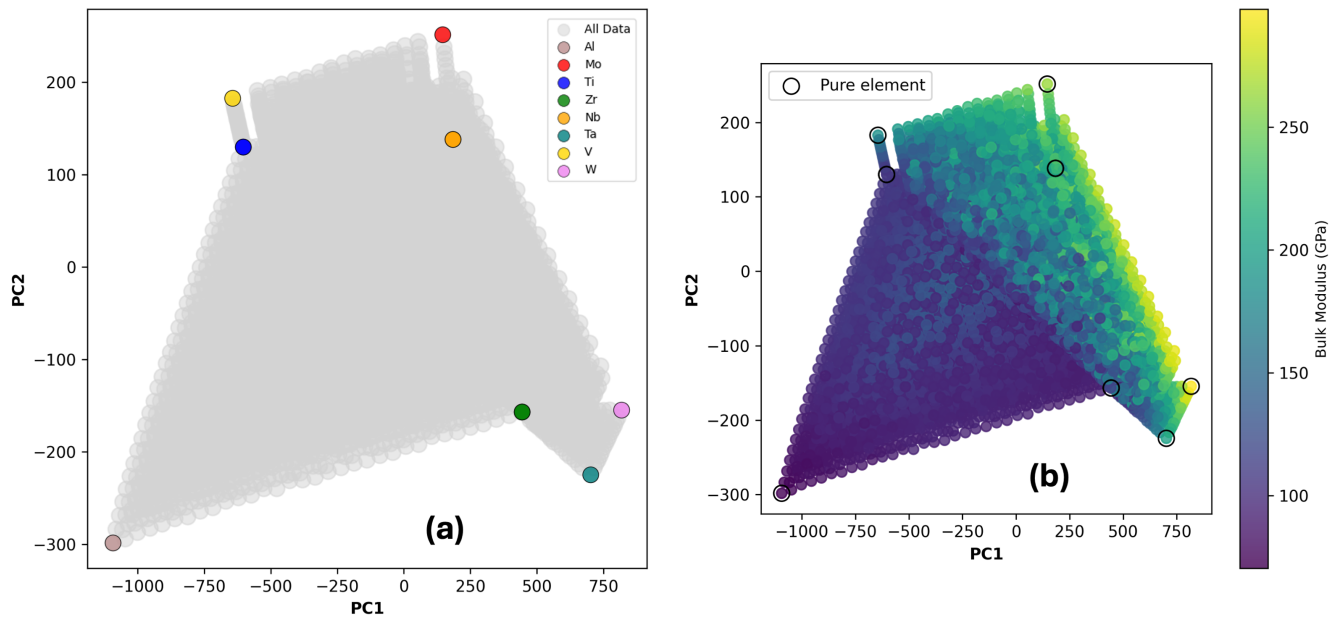


Fig. S2 Principal Component analysis of the combined compositional space. (a) The 2D projection of the pseudo-density feature vectors for both the training domain (\mathcal{D}_4) and the extrapolation domain (\mathcal{D}_7). (b) The same projection colored by Bulk Modulus. The overlap of the two datasets in the PC space confirms that the 7-component system does not occupy a distinct, disjoint region of the feature manifold, explaining the success of the extrapolative predictions.

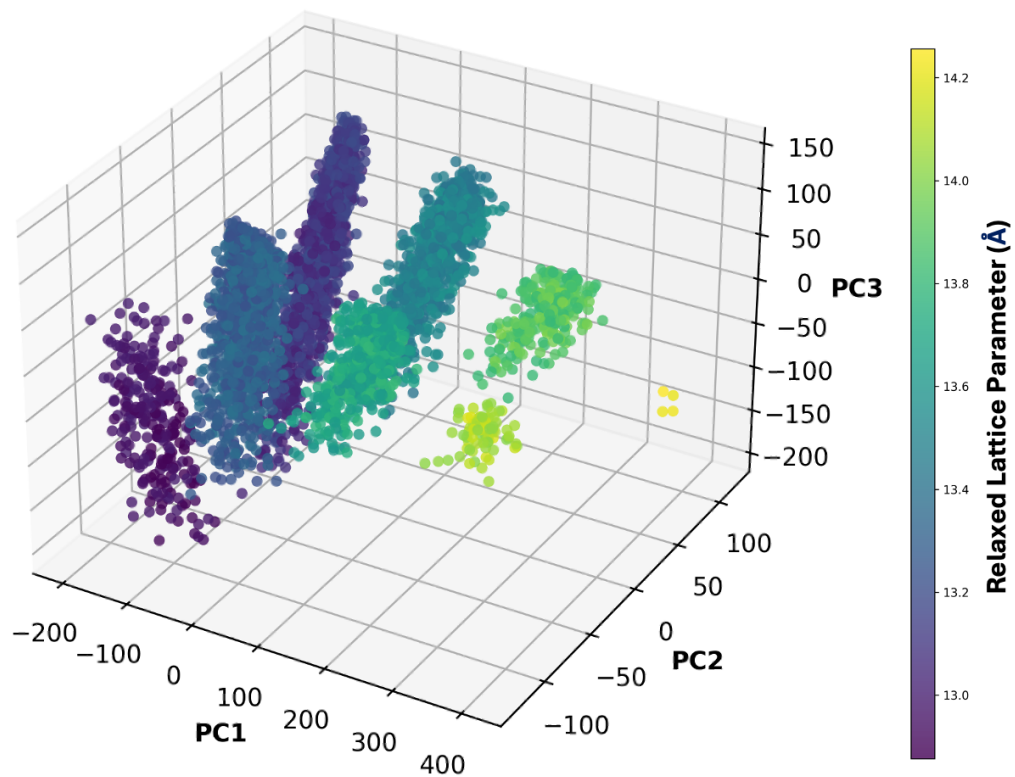


Fig. S3 Stratification of the relaxed manifold by cell volume. (shown \mathcal{D}_4 quaternary samples) The Principal Component space of the fully relaxed dataset colored by the final relaxed lattice parameter. The aggressive variance maximization of PCA captures the spatial dilation of the absolute-grid f_r , perfectly stratifying the disjoint branches by discrete lattice parameter bands ranging from 12.8 Å to 14.2 Å.

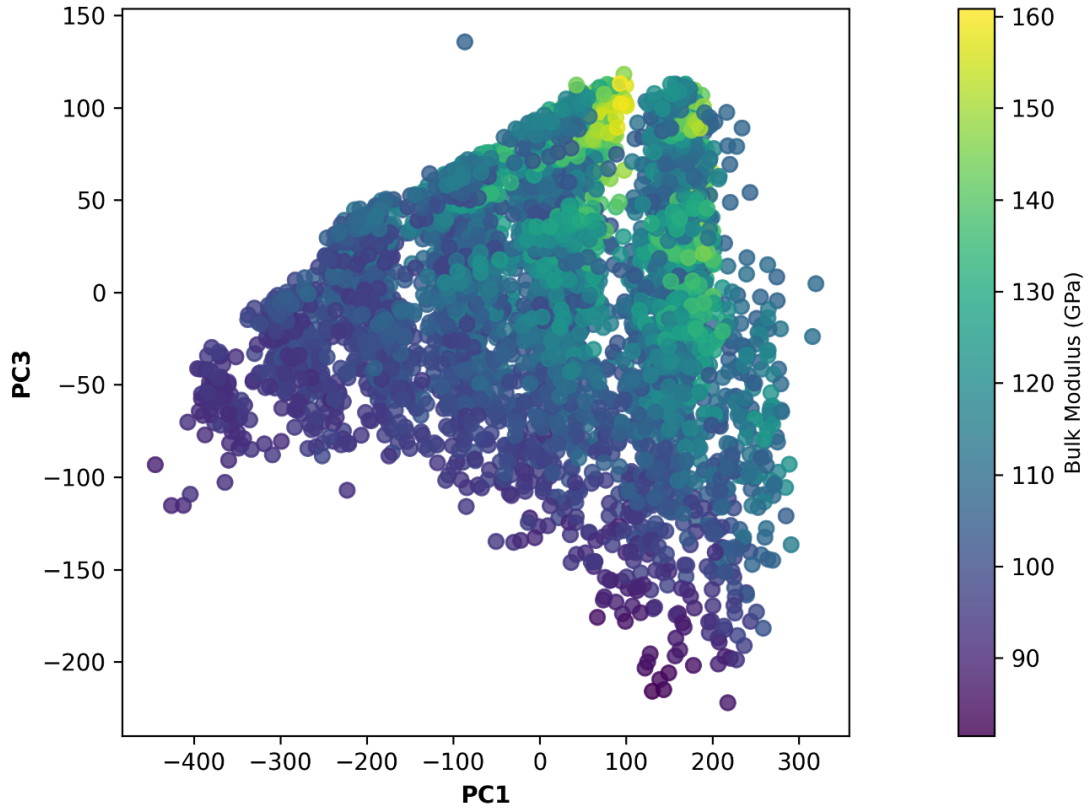


Fig. S4 Validation of volumetric scaling effects (shown \mathcal{D}_4 quaternary samples). When the absolute-grid 2-point spatial statistics (f_r) of the relaxed structures are divided by the cell volume (a^3) prior to PCA, the magnitude-dependent variance driven by global cell expansion is normalized. This suppression of volume-dependent information causes the previously disjoint, hyper-branched manifold to coalesce into a single, continuous cluster, confirming that non-uniform final lattice constants are the primary driver of the topological fracturing.

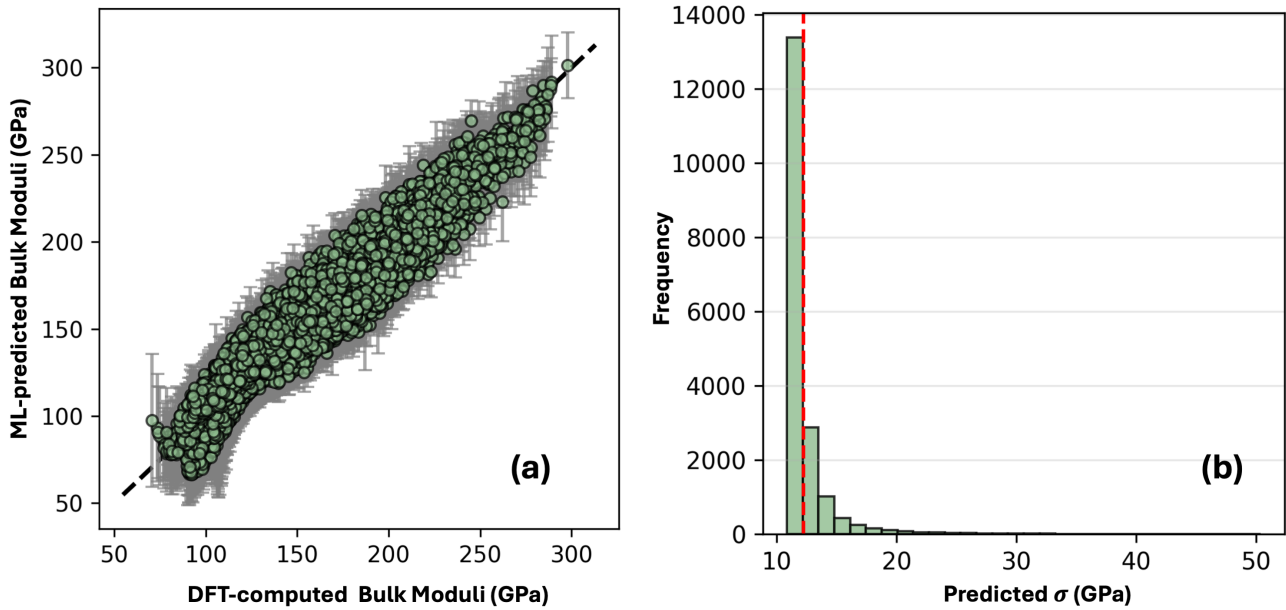


Fig. S5 Uncertainty quantification validation for extrapolation. (a) Parity plot and (b) uncertainty calibration histogram for the 7-component predictions. The well-calibrated uncertainty estimates indicate that the active learning acquisition function can effectively identify high-value candidates even in the unexplored extrapolation regime.

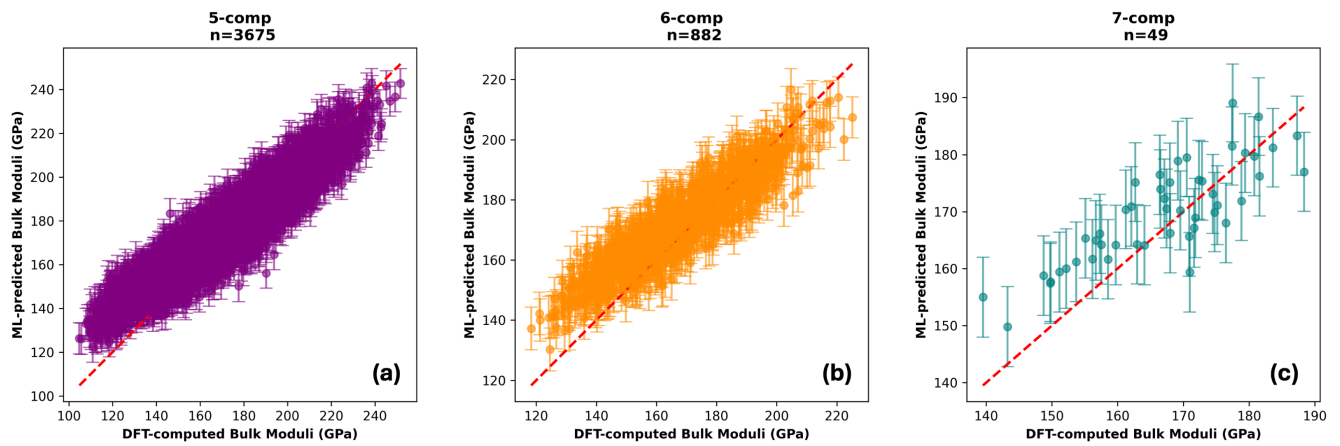


Fig. S6 Zero-shot extrapolative performance. Predictions for 5, 6, and 7-component alloys using the base model actively trained exclusively on a budget of 200 samples from the quaternary \mathcal{D}_4 system, with *no* exposure to Mo, Ta, V, or W. The preservation of the correlation trend ($y = x$) confirms that the physics of the refractory BCC manifold is learned solely from the lower-order system. These zero-shot predictions serve as the prior for the few-shot adaptation shown in the main text (Figure 6).

References

- 1 S. O. Jeje and M. B. Shongwe, *Engineering Reports*, 2025, **7**, e70141.
- 2 P. Dang, J. Hu, Y. Xian, C. Li, Y. Zhou, X. Ding, J. Sun and D. Xue, *Advanced Materials*, 2025, **37**, 2412198.
- 3 D. P. Tabor, L. M. Roch, S. K. Saikin, C. Kreisbeck, D. Sheberla, J. H. Montoya, S. Dwaraknath, M. Aykol, C. Ortiz, H. Tribukait, C. Amador-Bedolla, C. J. Brabec, B. Maruyama, K. A. Persson and A. Aspuru-Guzik, *Nature Reviews Materials*, 2018, **3**, 5–20.
- 4 W. Kohn and L. J. Sham, *Physical Review*, 1965, **140**, A1133–A1138.
- 5 P. Hohenberg and W. Kohn, *Physical Review*, 1964, **136**, B864–B871.
- 6 B. Chakraborty, P. Ray, N. Garg and S. Banerjee, *International Journal of Hydrogen Energy*, 2021, **46**, 4154–4167.
- 7 A. Kundu, A. Jaiswal, P. Ray, S. Sahu and B. Chakraborty, *Journal of Physics D: Applied Physics*, 2024, **57**, 495502.
- 8 H. T. Nair, A. Kundu, P. Ray, P. K. Jha and B. Chakraborty, *Sustainable Energy & Fuels*, 2023, **7**, 5109–5119.
- 9 S. Ramakrishna, T.-Y. Zhang, W.-C. Lu, Q. Qian, J. S. C. Low, J. H. R. Yune, D. Z. L. Tan, S. Bressan, S. Sanvito and S. R. Kalidindi, *Journal of Intelligent Manufacturing*, 2019, **30**, 2307–2326.
- 10 P. Ray, K. Choudhary and S. R. Kalidindi, *Integrating Materials and Manufacturing Innovation*, 2025, **14**, 1–13.
- 11 L. Ward, A. Agrawal, A. Choudhary and C. Wolverton, *npj Computational Materials*, 2016, **2**, 1–7.
- 12 L. Ward, A. Dunn, A. Faghaninia, N. E. R. Zimmermann, S. Bajaj, Q. Wang, J. Montoya, J. Chen, K. Bystrom, M. Dylla, K. Chard, M. Asta, K. A. Persson, G. J. Snyder, I. Foster and A. Jain, *Computational Materials Science*, 2018, **152**, 60–69.
- 13 P. Ray, A. R. Castillo, M. Kolel-Veetil and S. R. Kalidindi, *Advanced Science*, 2026, **n/a**, e23817.
- 14 X. Lei and A. J. Medford, *The Journal of Physical Chemistry Letters*, 2022, **13**, 7911–7919.
- 15 P. R. Kaundinya, K. Choudhary and S. R. Kalidindi, *JOM*, 2022, **74**, 1395–1405.
- 16 S. R. Kalidindi, A. J. Medford and D. L. McDowell, *JOM*, 2016, **68**, 2126–2137.
- 17 F. Brockherde, L. Vogt, L. Li, M. E. Tuckerman, K. Burke and K.-R. Müller, *Nature Communications*, 2017, **8**, 872.
- 18 T. Xie and J. C. Grossman, *Physical Review Letters*, 2018, **120**, 145301.
- 19 K. Choudhary and B. DeCost, *npj Computational Materials*, 2021, **7**, 1–8.
- 20 A. Merchant, S. Batzner, S. S. Schoenholz, M. Aykol, G. Cheon and E. D. Cubuk, *Nature*, 2023, **624**, 80–85.
- 21 A. P. Bartók, R. Kondor and G. Csányi, *Physical Review B*, 2013, **87**, 184115.
- 22 P. Lyngby, C. Larsen and K. W. Jacobsen, *Physical Review Materials*, 2024, **8**, 123802–123802.
- 23 A. G. Kusne, H. Yu, C. Wu, H. Zhang, J. Hatrnick-Simpers, B. DeCost, S. Sarker, C. Oses, C. Toher, S. Curtarolo, A. V. Davydov, R. Agarwal, L. A. Bendersky, M. Li, A. Mehta and I. Takeuchi, *Nature Communications*, 2020, **11**, 5966.
- 24 X. Qian, B.-J. Yoon, R. Arróyave, X. Qian and E. R. Dougherty, *Patterns*, 2023, **4**, 1–20.
- 25 T. Lookman, P. V. Balachandran, D. Xue and R. Yuan, *npj Computational Materials*, 2019, **5**, 21.
- 26 P. Ray, A. P. Generale, N. Vankireddy, Y. Asoma, M. Nakauchi, H. Lee, K. Yoshida, Y. Okuno and S. R. Kalidindi, *npj Computational Materials*, 2025, **11**, 234.
- 27 P. Ray, A. Yuichiro, N. Vankireddy, A. P. Generale, N. Masataka, L. Haein, Y. Katsuhisa, S. R. Kalidindi and O. Yoshishige, *Assessing the accuracy of Bayesian-optimized CGMD in predicting polymer miscibility*, 2025, <https://chemrxiv.org/engage/chemrxiv/article-details/69263681a10c9f5ca1c0700b>.
- 28 M. O. Buzzy, D. Montes de Oca Zapiain, A. P. Generale, S. R. Kalidindi and H. Lim, *Acta Materialia*, 2025, **284**, 120537.
- 29 D. Khatamsaz, B. Vela, P. Singh, D. D. Johnson, D. Allaire and R. Arróyave, *npj Computational Materials*, 2023, **9**, 49.
- 30 R. Nakayama, R. Shimizu, T. Haga, T. Kimura, Y. Ando, S. Kobayashi, N. Yasuo, M. Sekijima and T. Hitosugi, *Science and Technology of Advanced Materials: Methods*, 2022, **2**, 119–128.
- 31 J. Startt, M. J. McCarthy, M. A. Wood, S. Donegan and R. Dingreville, *npj Computational Materials*, 2024, **10**, 164.
- 32 Z. Hou and K. Tsuda, *Machine Learning Meets Quantum Physics*, Springer International Publishing, Cham, 2020, pp. 413–426.
- 33 P. I. Frazier, *A Tutorial on Bayesian Optimization*, 2018, <https://arxiv.org/abs/1807.02811>, Version Number: 1.
- 34 S. M. A. Alvi, J. Janssen, D. Khatamsaz, D. Perez, D. Allaire and R. Arróyave, *Acta Materialia*, 2025, **289**, 120908.
- 35 T. Hastie, J. Friedman and R. Tibshirani, *The Elements of Statistical Learning*, Springer New York, New York, NY, 2001.
- 36 C. E. Rasmussen and C. K. I. Williams, *Gaussian Processes for Machine Learning*, The MIT Press, 2005.
- 37 C. G. E. Boender and J. Mockus, *Mathematics of Computation*, 1991, p. 878.
- 38 J. Mockus, *Bayesian Approach to Global Optimization: Theory and Applications*, Springer Netherlands, Dordrecht, 1989.
- 39 K. Hanaoka, *iScience*, 2021, **24**, 1–19.
- 40 Y. Zhao, K. Yuan, Y. Liu, S.-Y. Louis, M. Hu and J. Hu, *The Journal of Physical Chemistry C*, 2020, **124**, 17262–17273.
- 41 A. D. Casey, S. F. Son, I. Bilonis and B. C. Barnes, *Journal of Chemical Information and Modeling*, 2020, **60**, 4457–4473.
- 42 M. C. Barry, *Ph.D.*, Georgia Institute of Technology, United States – Georgia, 2023.
- 43 M. C. Barry, K. E. Wise, S. R. Kalidindi and S. Kumar, *The Journal of Physical Chemistry Letters*, 2020, **11**, 9093–9099.
- 44 M. C. Barry, J. R. Gissinger, M. Chandross, K. E. Wise, S. R. Kalidindi and S. Kumar, *Computational Materials Science*, 2023, **230**, 112431.
- 45 M. C. Barry, S. Kumar and S. R. Kalidindi, *Machine Learning in*

- Molecular Sciences*, Springer International Publishing, Cham, 2023, vol. 36, pp. 67–89.
- 46 S. R. Kalidindi, *Hierarchical Materials Informatics*, Elsevier, 2015.
- 47 P. R. Kaundinya, K. Choudhary and S. R. Kalidindi, *Physical Review Materials*, 2021, **5**, 063802.
- 48 A. Cecen, H. Dai, Y. C. Yabansu, S. R. Kalidindi and L. Song, *Acta Materialia*, 2018, **146**, 76–84.
- 49 A. Mann and S. R. Kalidindi, *Frontiers in Materials*, 2022, **9**, 1–14.
- 50 A. Zunger, S.-H. Wei, L. G. Ferreira and J. E. Bernard, *Physical Review Letters*, 1990, **65**, 353–356.
- 51 O. Čertík, J. E. Pask and J. Vackář, *Computer Physics Communications*, 2013, **184**, 1777–1791.
- 52 S. Bhowmik, J. E. Pask, A. J. Medford and P. Suryanarayana, *Computer Physics Communications*, 2025, **308**, 109448.
- 53 A. van de Walle, M. Asta and G. Ceder, *Calphad*, 2002, **26**, 539–553.
- 54 D. Gehringer, M. Friák and D. Holec, *Computer Physics Communications*, 2023, **286**, 108664.
- 55 D. R. Hamann, *Physical Review B*, 2013, **88**, 085117.
- 56 M. F. Shojaei, J. E. Pask, A. J. Medford and P. Suryanarayana, *Computer Physics Communications*, 2023, **283**, 108594.
- 57 J. P. Perdew, K. Burke and M. Ernzerhof, *Physical Review Letters*, 1996, **77**, 3865–3868.
- 58 B. Zhang, X. Jing, S. Kumar and P. Suryanarayana, *SoftwareX*, 2023, **21**, 101295.
- 59 Q. Xu, A. Sharma and P. Suryanarayana, *SoftwareX*, 2020, **11**, 100423.
- 60 B. Zhang, X. Jing, Q. Xu, S. Kumar, A. Sharma, L. Erlandson, S. J. Sahoo, E. Chow, A. J. Medford, J. E. Pask and P. Suryanarayana, *Software Impacts*, 2024, **20**, 100649.
- 61 Q. Xu, A. Sharma, B. Comer, H. Huang, E. Chow, A. J. Medford, J. E. Pask and P. Suryanarayana, *SoftwareX*, 2021, **15**, 100709.
- 62 F. Ren and F. Liu, *The Journal of Chemical Physics*, 2022, **157**, 184106.
- 63 D. T. Fullwood, S. R. Kalidindi, S. R. Niezgoda, A. Fast and N. Hampson, *Materials Science and Engineering: A*, 2008, **494**, 68–72.
- 64 T. Fast and S. R. Kalidindi, *Acta Materialia*, 2011, **59**, 4595–4605.
- 65 S. R. Niezgoda, D. T. Fullwood and S. R. Kalidindi, *Acta Materialia*, 2008, **56**, 5285–5292.
- 66 S. R. Niezgoda, Y. C. Yabansu and S. R. Kalidindi, *Acta Materialia*, 2011, **59**, 6387–6400.
- 67 G. Kresse and J. Hafner, *Physical Review B*, 1993, **47**, 558–561.
- 68 G. Kresse and J. Furthmüller, *Computational Materials Science*, 1996, **6**, 15–50.
- 69 G. Kresse and J. Furthmüller, *Physical Review B*, 1996, **54**, 11169–11186.
- 70 G. Kresse and D. Joubert, *Physical Review B*, 1999, **59**, 1758–1775.
- 71 S. Maes, F. D. Ceuster, M. V. d. Sande and L. Decin, *Journal of Open Source Software*, 2025, **10**, 7148.
- 72 C. E. Rasmussen and H. Nickisch, *Journal of Machine Learning Research*, 2010, **11**, 3011–3015.
- 73 C. E. Rasmussen and C. K. I. Williams, *Gaussian processes for machine learning*, MIT Press, Cambridge, Mass, 2006.
- 74 D. V. Lindley, *The Annals of Mathematical Statistics*, 1956, **27**, 986–1005.
- 75 X. Huan and Y. M. Marzouk, *Journal of Computational Physics*, 2013, **232**, 288–317.
- 76 S. Kumar, X. Jing, J. E. Pask, A. J. Medford and P. Suryanarayana, *The Journal of Chemical Physics*, 2023, **159**, 244106.
- 77 L. R. Timmerman, S. Kumar, P. Suryanarayana and A. J. Medford, *Journal of Chemical Theory and Computation*, 2024, **20**, 5788–5795.